ISSN 0023-1584, Kinetics and Catalysis, 2007, Vol. 48, No. 1, pp. 116–124. © MAIK "Nauka/Interperiodica" (Russia), 2007.
Original Russian Text © M.M. Danilova, Z.A. Sabirova, N.A. Kuzin, V.A. Kirillov, N.A. Rudina, E.M. Moroz, A.I. Boronin, 2007, published in Kinetika i Kataliz, 2007, Vol. 48, No. 1, pp. 123–131.

Reinforced Nickel and Nickel–Platinum Catalysts for Performing the Thermally Coupled Reactions of Methane Steam Reforming and Hydrogen Oxidation

M. M. Danilova, Z. A. Sabirova, N. A. Kuzin, V. A. Kirillov, N. A. Rudina, E. M. Moroz, and A. I. Boronin

Boreskov Institute of Catalysis, Siberian Branch, Russian Academy of Sciences, Novosibirsk, 630090 Russia
E-mail: sabirova@catalysis.nsk.su

Received June 30, 2005

Abstract—The formation of composite nickel and nickel–platinum catalysts reinforced with steel gauze was studied. The catalysts were prepared by sintering powdered nickel metal and a supported nickel catalyst (GIAP-3 or NIAP-18) with a chromium oxide additive in the case of nickel-containing composite catalysts or by sintering powdered nickel, aluminum, and a supported platinum catalyst in the case of catalysts containing nickel–platinum. With the use of electron microscopy, mercury porosimetry, and X-ray electron probe microanalysis, it was found that a metal matrix, in the pores of which supported catalyst particles were distributed, was formed in the composite catalysts. The reinforced nickel catalysts prepared were active in the reaction of methane steam reforming, and the catalysts containing nickel–platinum were active in the reaction of hydrogen oxidation. An increase in the activity of reinforced nickel catalysts in the course of the reaction was found. It is believed that the increase of the activity was due to the reduction of nickel oxide from an inactive difficult-to-reduce oxide film containing nickel and chromium oxides under the action of the reaction atmosphere.

DOI: 10.1134/S0023158407010156

INTRODUCTION

A new area of power engineering—fuel cells in which hydrogen is electrochemically oxidized with oxygen—has been intensively developed in the past decade. The steam reforming of methane or liquid hydrocarbon fuels is a preferable hydrogen generation technique. The greatest effect in the operation of fuel cells can be reached by performing the endothermic reaction of methane steam reforming simultaneously with the exothermic reaction of the oxidation of spent anode gas, which contains unreacted hydrogen. An approach to solving this problem is to use catalytic heat-exchange reactors coupled through the heat flows of the above reactions. The main element of the heat-exchange reactors is a metal wall on one side of which a catalyst for the methane steam reforming reaction is distributed, and a catalyst for the exothermic reaction of the oxidation of anode gases in a fuel-cell battery is located on the other side [1].

The reaction of methane steam reforming performed with the use of catalytic heat-exchange reactors was considered in a number of publications [1–4]. Kirillov et al. [1] reported the results of testing a plate heat-exchange reactor with the use of reinforced composite catalysts on metal heat-exchange surfaces: nickel and platinum for the reactions of steam reforming and hydrogen oxidation, respectively.

Polman et al. [2] used a reactor made of flat and corrugated stainless steel plates with supported catalysts as thin layers for performing the thermally coupled reactions of endothermic methane steam reforming and exothermic methane combustion. Ismagilov et al. [3, 4] used a tube-type reactor. A catalyst containing a porous nickel–chromium support with an alumina sublayer and a supported perovskite or platinum catalyst for the combustion of methane or a mixture of methane with hydrogen was distributed over the outer surface of a tube, and a catalyst that consisted of a porous nickel support with an oxide sublayer and supported nickel was arranged on the inner surface of the tube.

In this work, we studied the formation of composite catalysts containing nickel and nickel–platinum reinforced with stainless steel gauze and the catalytic properties of the nickel and nickel–platinum catalysts in the reactions of methane steam reforming and hydrogen oxidation, respectively.

EXPERIMENTAL

The catalysts were prepared in accordance with a previously published procedure [5, 6]. To prepare reinforced composite nickel catalysts, a mixture of components containing nickel metal powder (PNE-1), a commercial GIAP-3 [7] or NIAP-18 [8] catalyst (particle size smaller than 0.25 mm), and chromium oxide (84.0–85.5 wt % Ni, 12.5 wt % commercial catalyst,

and 2.0–3.5 wt % chromium oxide) was mixed with a rubber-based adhesive and applied to reinforcing gauze. The adhesive content of the catalyst bed separated from the reinforcing gauze was ~4 wt % in terms of dry substance. The reinforced composite nickel–platinum catalysts were prepared by supporting a mixture of components containing 70.0 wt % nickel metal, 18.0 wt % aluminum powder (PAVCh), and 12.0 wt % supported catalyst (0.6 wt % Pt/Al_2O_3) in an organic adhesive onto reinforcing gauze. The supported platinum catalyst was prepared by impregnating γ-Al_2O_3 (spheres of size 0.8–1.2 mm) with a specific surface area of 150 m^2/g with a solution of H_2PtCl_6 in hydrochloric acid followed by drying, heating at 450°C in a flow of N_2, and reduction at 950°C in a flow of H_2; the reduction temperature was chosen for more completely removing Cl^- ions from the catalyst surface [9]. The reinforced catalysts were sintered in a vacuum oven at 760°C for 2 h.

The particle-size analysis of the catalysts, which was performed using sieves with mesh dimensions of 0.25, 0.20, 0.10, and 0.045 mm, demonstrated that fractions of 0.20–0.10 and 0.10–0.045 mm were predominant in GIAP-3 and NIAP-18 catalysts, respectively; in the 0.6% Pt/Al_2O_3 catalyst, a fraction finer than 0.045 mm was present in considerable amounts in addition to the above fractions.

According to data obtained by scanning electron microscopy (SEM), the predominant particle sizes of aluminum, nickel, and chromium oxide powders were 3–15, 10–25, and 0.3–0.7 μm, respectively.

The specific surface areas of catalysts were determined by the BET method from the thermal desorption of argon. The total pore volume and pore-size distribution were determined by mercury porosimetry. The size and shape of particles were determined by SEM and transmission electron microscopy (TEM) on REM-100U and JEM-100CX instruments, respectively.

X-ray electron probe microanalysis was performed with the use of a LEO-420 scanning microscope with a RONTEK X-ray microanalyzer.

X-ray diffraction (XRD) analysis was performed using diffraction patterns taken on an HZY-4 instrument (monochromatic CuK_α radiation). The specific surface area of platinum (S_{Pt}) was determined by gas chromatography from the selective chemisorption of oxygen at room temperature.

The XPS spectra were measured on an ES300 electron spectrometer from Kratos Analytical with the use of MgK_α X-ray radiation ($h\nu$ = 1253.6 eV); the mean free path of electrons λ was 20–30 Å depending on the test line. Correspondingly, the averaged test surface thickness of samples was equal to 2–3 λ, that is, 40–60 Å. The samples were fixed in a holder with the use of vacuum-resistant, two-sided adhesive tape. Before spectroscopic measurements, the samples were pumped to $P = 10^{-7}$ mbar; in the course of measurements, the vacuum was no worse than 10^{-8} mbar. The main background gases were CO, CO_2, and H_2O. The transmission energy was 75 or 25 eV for measuring a survey spectrum or individual lines, respectively. The scale of binding energies was precalibrated with a test sample of gold, copper, and silver foils using the Au $4f_{7/2}$ (84.0 eV), Ag $3d_{5/2}$ (368.3 eV), and Cu $2p_{3/2}$ (932.7 eV) lines [10]. The surface composition was calculated from integrated line intensities with consideration for atomic sensitivity factors [11].

The positions of the Al 2*p* and C 1*s* lines were used as references for the calibration of the spectra of test samples [10, 11]. The presence of nickel, chromium, aluminum, carbon, oxygen, and calcium was detected in catalyst bed samples based on NIAP-18. After catalytic tests, the XPS spectra exhibited additional lines of Si; it is likely that these lines resulted from quartz impurities in the sample from glass fiber used for the fixation of the catalyst bed in the reactor. In all of the above studies, composite catalysts separated from reinforcing gauze were used.

The activity of catalysts in the reaction of methane steam reforming was determined using a flow-circulation setup with a stainless steel reactor (volume of 34 cm^3; diameter of 22 mm) at atmospheric pressure, the molar ratio $H_2O/CH_4 = 2.0$, and 750°C; the flow rate was 11.8 l/h. The reinforced catalysts were tested as plates (of size $20 \times 31.8 \times 1.1$ mm; volume of 0.7 cm^3) or a fraction of the catalyst bed separated from reinforcing gauze (0.25–0.50 mm; weighed portion of 0.8 g); the commercial catalysts were tested as a fraction (0.25–0.50 mm; weighed portion of 0.8 g) or as the halves of natural grains (volume of 0.7 cm^3; GIAP-3 as a cylinder 1.08 cm in diameter and 0.78 cm in height; NIAP-18 as a hollow cylinder 1.50 and 0.60 cm in external and internal diameters, respectively, and 0.48 cm in height). Before activity measurements, the samples were reduced in a flow of H_2 at 750°C for 1 h; then, hydrogen was replaced by a reaction mixture, and the measurements were performed after an exposure to the reaction mixture for 1 h. The composition of reaction mixtures was analyzed by chromatography.

The activity of catalysts in the reaction of hydrogen oxidation was determined in the above flow-circulation setup at atmospheric pressure. The starting mixture containing 1.2 vol % H_2, 2.5 vol % N_2, and 96.3 vol % O_2 was supplied at a flow rate of 10.0 l/h. A supported catalyst was tested as a fraction (0.25–0.50 mm; weighed portion of 0.5 g); a reinforced catalyst was tested as plates (of size $20 \times 31.8 \times 1.1$ mm; volume of 0.7 cm^3) and a fraction of the catalyst bed separated from reinforcing gauze (0.25–0.50 mm; weighed portion of 0.5 g). The test catalyst was placed in a reactor with quartz. Before activity measurements, the catalyst was heated at 400°C for 2 h in a mixture containing 98 vol % O_2 and 2 vol % N_2 in order to form a surface layer corresponding to an excess of oxygen in the reaction mixture [12]. Next, the sample was cooled to 80°C, and a reaction mixture was supplied. The com-

Table 1. Unit-cell parameter (a) and particle size (D) of NiO in the 12.5% NIAP-18 + 84.0% Ni + 3.5% Cr_2O_3 catalyst

Treatment conditions	a_{NiO}, Å	D_{NiO}, Å
Initial (760°C; vacuum oven)	4.161	95
Reduced (750°C; H_2)	4.138	330
After reaction	4.138	330

position of the reaction mixture was analyzed by chromatography.

RESULTS AND DISCUSSION

Phase Composition and Texture of Nickel-Containing Catalysts

According to XRD data, the composite catalysts contained the phases of Ni, α-Cr_2O_3, and α-Al_2O_3; the sample based on NIAP-18 additionally contained $CaO \cdot 6Al_2O_3$ phases and a small amount of a solid solution of chromium oxide in nickel oxide with the unit-cell parameter ranging from 4.161 to 4.138 Å depending on treatment conditions (Table 1). According to reference data, the unit-cell parameter of NiO is 4.177 Å [13]. The NiO phase was detected based on the presence of three weak diffraction peaks: (111), (200), and (220). It is likely that the fraction of the solid solution of chromium oxide in nickel oxide in composite catalyst samples based on GIAP-3 containing 2.0 wt % Cr_2O_3 was small and the solid solution was not detected using XRD; the NiO phase was absent.

Table 2 summarizes the characteristics of the pore structure of nickel composite catalysts. The samples exhibited a coarse-pored structure: according to mercury porosimetry data, pores with radii from 15 to 100 μm were responsible for the main pore volume (Fig. 1). According to SEM data, the catalyst was a coarse-pored material with a corpuscular structure intergrown by spherical conglomerates of size 5–15 μm united at contact sites (Fig. 2a, arrow A). Either irregularly shaped individual particles of size 1–3 μm (Fig. 2a, arrow B) or the aggregates of small particles (particle size of 0.3–1 μm; aggregate size of 1–5 μm) (Fig. 2a, arrow C) were distributed in the pores. The elemental composition of morphologically different formations determined by X-ray electron probe microanalysis demonstrated that the coarse spherical conglomerates united at contact sites to form the framework of a composite catalyst consisting mainly of nickel metal (90–95 wt %). Either individual particles of a supported nickel catalyst (Fig. 2a, arrow B; arrow D marks supported nickel) or a mixture of the supported catalyst with fine particles of nickel metal from powder and chromium oxide (Fig. 2a, arrow C) were arranged in pores. In addition to these aggregates, chromium oxide was also detected in small amounts (1–5 wt %) in all of the test regions. A comparison of the electron micrographs of the parent nickel powder [14] and the composite catalyst demonstrated that the corpuscular porous structure was retained in the composite catalyst: structural elements of the parent nickel powder can be seen.

Based on earlier data [15], it is believed that a hydrocarbon from rubber reduced the film of nickel oxide on nickel particles from powder to metal on heating in a vacuum oven in the course of catalyst preparation. Evidently, the reduction was accompanied by the agglomeration of nickel particles and intergrowth at contact sites [16]; as a result of this, a metal matrix and a strong metal composite were formed.

After the combustion of carbon deposits under the action of oxygen from residual gases, an oxide film was formed on nickel metal. In the course of heating, this oxide film could interact with chromium oxide.

We did not detect relatively coarse particles (larger than 5–10 μm) of the supported nickel catalyst using SEM. This fact can be due to additional catalyst particle size reduction due to microcracking in the course of disintegration as a result of the wedging action of a liquid in contact with a liquid adhesive.

We evaluated the average particle size of supported nickel in the commercial and composite catalysts using TEM and found that the nickel particle size increased by a factor of 1.5–2 in the course of preparation (Table 2).

Table 2. Characteristics of nickel catalysts*

Catalyst	S_{sp}, m^2/g	Pore volume, cm^3/g			D_{Ni}, Å**
		$r < 10^3$ Å	$r = 10^3$–10^5 Å	$r > 10^5$ Å	
GIAP-3 (7.0% Ni on α-Al_2O_3)	6.3	0.10	0.05	0.06	100–200
12.5% GIAP-3 + 85.5% Ni + 2.0% Cr_2O_3	3.4	0.01	0.15	0.35	200–300
NIAP-18 (10.5% Ni/α-Al_2O_3)	12	0.09	0.13	0.08	100–200
12.5% NIAP-18 + 84.0% Ni + 3.5% Cr_2O_3	4.5	0.06	0.12	0.15	250–400

*Data for the reduced catalysts are given.

**D_{Ni} is the particle size of supported nickel according to TEM data.

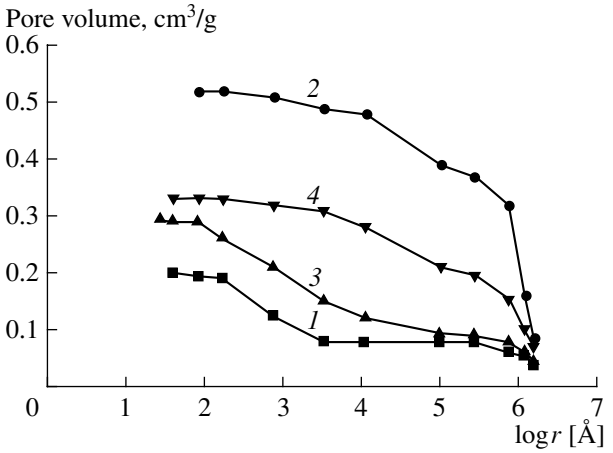

Fig. 1. Pore radius distribution: (*1*) GIAP-3 catalyst, (*2*) composite catalyst based on GIAP-3, (*3*) NIAP-18 catalyst, and (*4*) composite catalyst based on NIAP-18.

XPS Characterization of Nickel-Containing Catalysts

The following three samples of the composite catalyst based on NIAP-18 were studied by XPS using Ni 2*p*, Cr 2*p*, Al 2*p*, and C 1*s* lines: starting and reduced catalyst samples and a sample after testing in the reaction. Figure 3 shows the Ni 2*p* XPS spectra, whose shape is indicative of the presence of both metal and oxide components. The line at E_b ~ 853 eV corresponds to the metal state of nickel, whereas lines with E_b ~ 856 and ~862 eV correspond to oxide components. Note that the line with E_b ~ 862 eV is a satellite line from nickel in an oxide state. The positions of lines due to NiO_x correspond to trivalent nickel [11].

To obtain detailed information, we performed the deconvolution of the Ni 2*p* and Cr 2*p* spectra into individual components using the WinCalc software (Fig. 4). The Ni 2*p* spectra were described by three peaks, two of which with binding energies of 856.4 and 862.0 eV corresponded to an oxide state of nickel, Ni^{3+}. The contribution of the metal state became much higher upon the reduction of the sample and the action of the reaction atmosphere. In this case, the positions of the components of the Ni 2*p* spectrum remained almost unchanged; this fact suggests that analogous phases of reduced and oxide nickel were characteristic of all three samples. Note that, as compared with the spectra of the first two samples, the difference between the peaks of metal and oxide nickel decreased by 0.5 eV in the spectrum of the sample taken after catalytic tests. This suggests that, in this sample, the surface structures of both reduced nickel and an oxide phase were somewhat different; this was likely due to changes in the degree of imperfection and in the oxygen environment. The Cr 2*p* spectra consisted of two spin-orbital components 3/2 and 1/2. The Cr 2*p* spectra were decomposed into two components (within each spin-orbital component) with E_b = 576.6 ± 0.2 (Cr(A)) and 578.4 ± 0.2 eV (Cr(B)) (Fig. 4b). Both of the components belonged to the state

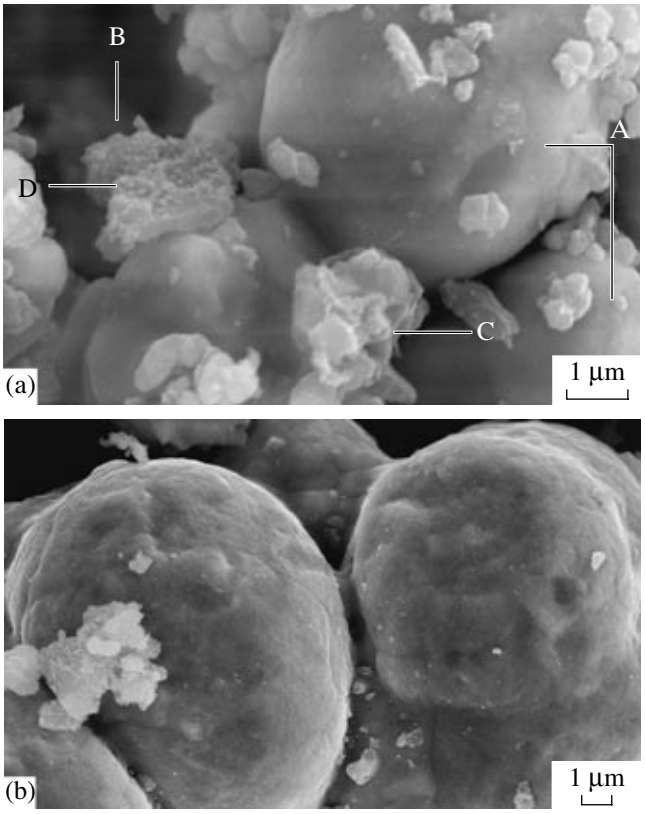

Fig. 2. Electron micrographs of reduced composite catalysts based on (a) GIAP-3 and (b) NIAP-18.

Cr^{3+}; however, the Cr^{3+} ions occurred in different structural positions [11, 17, 18]. The ratio between components changed on going from sample to sample. Thus, it can be seen that the intensity ratio between components with E_b = 578.4 ± 0.2 (Cr(B)) and 576.6 ± 0.2 eV (Cr(A)) increased from 0.17 to 0.3 and 0.25 upon the

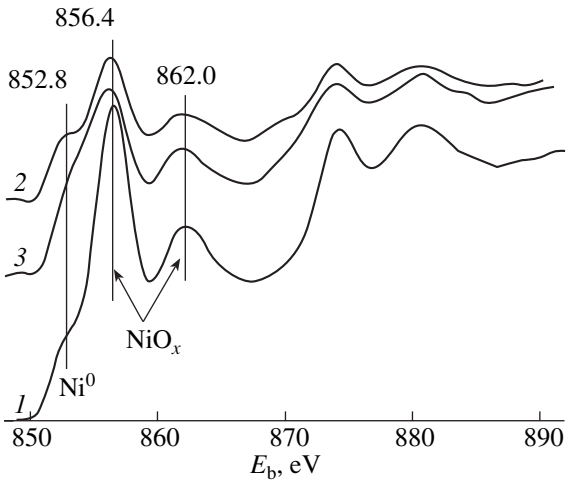

Fig. 3. The Ni 2*p* XPS spectrum of the composite catalyst based on NIAP-18: (*1*) initial sample, (*2*) reduced sample, and (*3*) sample after reaction.

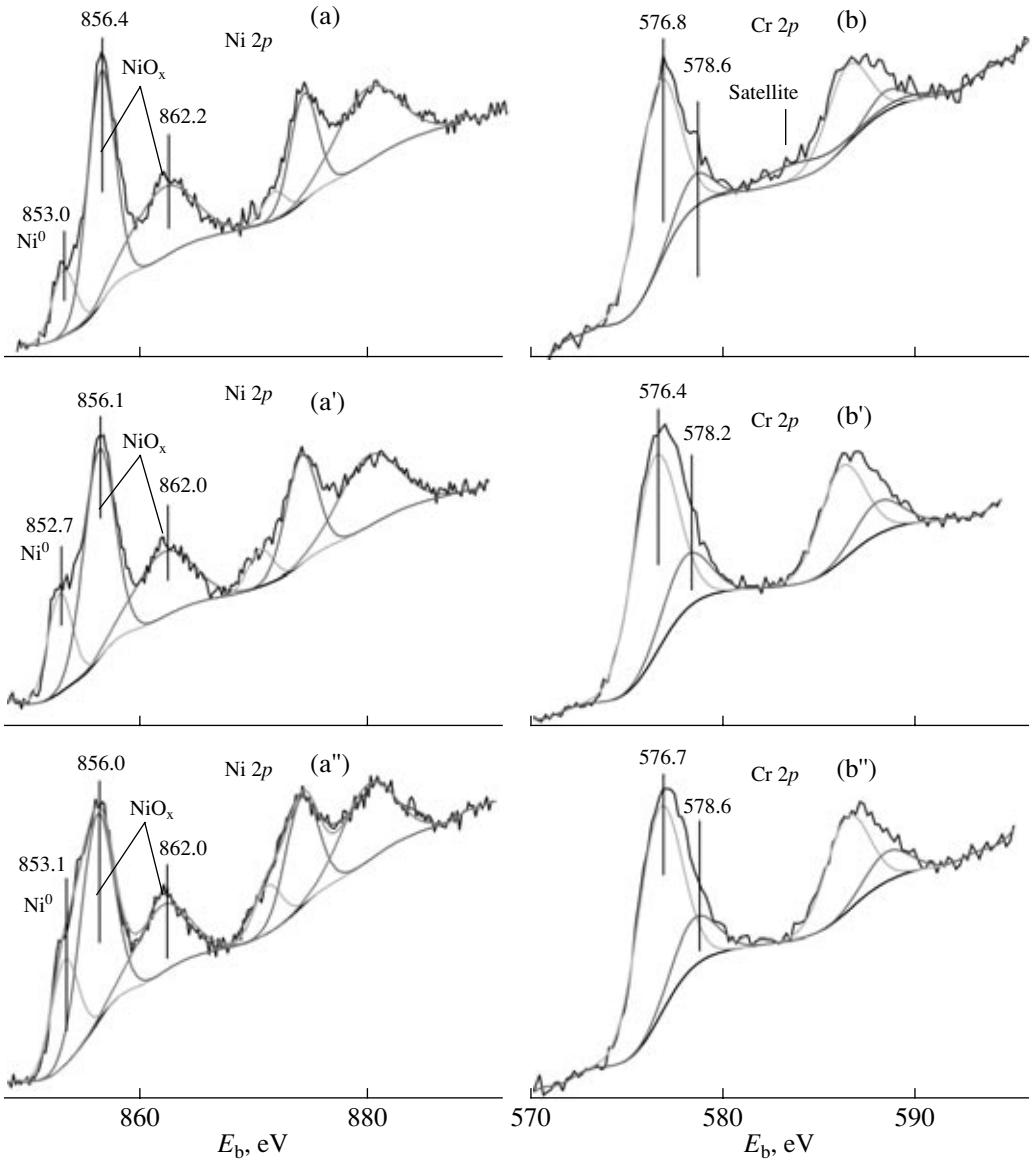

Fig. 4. Deconvolution of the (a, a', a") Ni 2*p* and (b, b', b") Cr 2*p* XPS spectra into components: (a, b) initial sample, (a', b') reduced sample, and (a", b") sample after reaction.

action of reducing and reaction atmospheres, respectively. The given ratio between the components Cr(B) and Cr(A) correlates with the effect of sample charging in the course of recording photoelectron spectra ($\Delta\Phi$). This effect had the following values in the order initial sample–reduced sample–sample exposed to a reaction atmosphere: 1.1, 2.8, and 2.1 eV. An increase in the effect of sample charging suggests an increase in the surface dielectric properties of the material. Taking into account these two facts, we believe that the increase in the Cr(B)/Cr(A) component ratio was due to the formation of a dielectric phase on the surface of nickel particles; this phase coated the metal phase of nickel. Surface oxide solid solutions can constitute this phase. The insertion of chromium ions into a nickel oxide film was accompanied by a decrease in the concentration of charge carriers in a near-surface layer. In the coordination sphere of oxygen, a greater or smaller amount of difficult-to-reduce chromium appeared along with easy-to-reduce nickel. As a result of this, the reactivity of oxygen decreased (the heat of formation of chromium oxide is higher than that of nickel oxide [19]). It is believed that the interaction of chromium oxide with nickel oxide occurred even in the course of catalyst preparation at the stage of high-temperature treatment (760°C; vacuum oven); this interaction was intensified under the action of a reducing atmosphere in the course of hydrogen treatment (750°C; H_2) before the reaction. The decrease in the unit-cell parameter of NiO in the composite catalyst (Table 1) is indicative of the interac-

Table 3. Texture characteristics of platinum catalysts

Catalyst	S_{sp}, m^2/g	Pore volume, cm^3/g			S_{Pt}, $m^2/(g\ Cat)$
		$r < 10^3$ Å	$r = 10^3$–10^5 Å	$r > 10^5$ Å	
0.6% Pt/Al_2O_3	127	0.54	0.01	0.04	2.3
12% (0.6% Pt/Al_2O_3) catalyst + 70.0% Ni + 18.0% Al	3.6	0.03	0.11	0.17	–

tion of nickel oxide with chromium oxide. It is likely that a component of the Cr 2*p* spectrum with the binding energy of 578.4 ± 0.2 eV belongs to the Cr^{3+} ion, which is a constituent of the lattice of NiO. Because of the interaction of nickel oxide with difficult-to-reduce chromium oxide, the agglomeration of nickel metal formed upon reduction is hindered and the dispersity of nickel metal increases [20–22].

The fact that, according to XPS data, the Ni^{3+} state corresponds to nickel in an oxide state, whereas a solid solution phase based on NiO was detected by XRD analysis, can be explained by taking into account that XRD analysis provides information on the entire volume of the catalyst, whereas XPS provides information on the surface. The states of oxide nickel can be different on the catalyst surface and in the bulk. Moreover, note that the shape of the Ni 2*p* spectrum is complicated and the superposition of spectra from Ni^{3+} and Ni^{2+}(NiO) may occur in these samples. It was impossible to distinguish the individual spectra of Ni^{3+} and Ni^{2+}.

Phase Composition and Texture of Nickel–Platinum Catalysts

According to XRD data, γ- and δ-Al_2O_3 species were detected in the supported platinum catalyst (Pt/Al_2O_3) and Ni_3Al and $Al_{1.1}Ni_{0.9}$ phases were detected in the composite catalyst. Table 3 summarizes the texture characteristics of the catalysts. The catalyst containing nickel–platinum exhibited a coarse-pored structure: according to mercury porosimetry data, the predominant pore radius was 15–70 μm (Table 3). The coarse-pored structure is consistent with SEM data. The sample was a material that underwent intense agglomeration: conglomerates that constitute a metal matrix (Fig. 5, arrow A) grew together to form a body with a sponge pore structure. Irregularly shaped supported platinum catalyst particles of size 0.5–5 μm were distributed in the pores (Fig. 5, arrow B). Agglomeration was enhanced upon the introduction of aluminum because the agglomeration of the nickel–aluminum system occurred in the presence of a liquid phase of molten aluminum ($T_{m,Al}$ = 660°C). According to published data [23, 24], the resulting molten aluminum rapidly spread over the surface of nickel particles. This dramatically increased the surface area of the interaction of components to accelerate the formation of intermetallides; consequently, the temperature sharply increased (the heats of formation ($-\Delta H$) of the solid chemical compounds of nickel with aluminum Ni_3Al and NiAl are 37.6 and 34.0 kcal/mol, respectively [25]). The formation of nickel–aluminum metal supports was considered previously [14].

Supported platinum catalyst particles larger than 5–10 μm were not detected in the catalyst by SEM.

Catalytic Activity of Nickel-Containing Catalysts

Reinforced nickel catalysts were tested in the reaction of methane steam reforming. The determination of the catalytic activity of reinforcing gauze separated from a catalytic layer demonstrated that the degree of conversion on it was no higher than 1%, which is comparable to the degree of conversion in the empty reactor. Figure 6 shows the dependence of the conversion of methane on reaction time for reinforced and commercial catalysts. The conversion of methane on commercial catalysts after reduction immediately exhibited the highest value (curves *1*, *2*). It slowly decreased (by ~10 rel %) in the course of the reaction. Another character of activity changes with reaction time was observed on reinforced catalysts (Fig. 6, curves *3*, *4*). In the initial period of the reaction, the extents of conversion were low (10–15%); however, they increased under the reaction conditions and reached a maximum value after ~10 h. After reaching the maximum value, the activity of catalysts remained stable over the entire period of testing (40 h). Low conversions during the initial period of the reaction can be explained by the fact that an inactive oxide

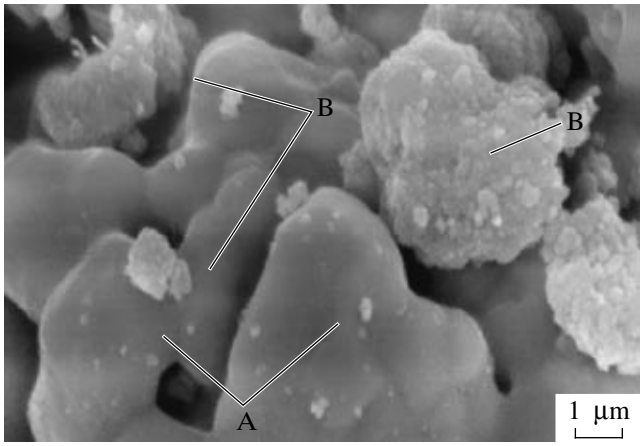

Fig. 5. Electron micrograph of the composite nickel–platinum catalyst: (A) metal matrix and (B) Pt/Al_2O_3.

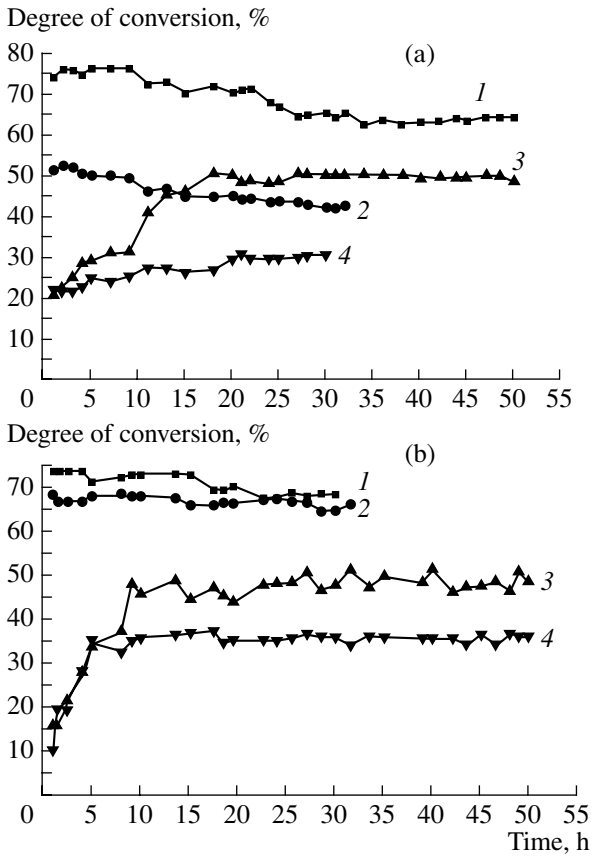

Fig. 6. Effect of the duration of testing on the degree of methane conversion in the reaction of methane steam reforming on the following samples containing commercial (a) GIAP-3 and (b) NIAP-18 catalysts: (a) (*1*) GIAP-3 (fraction of 0.25–0.50 mm), (*2*) GIAP-3 (1/2 grain; cylinder), (*3*) reinforced catalyst based on GIAP-3 (plate), and (*4*) catalytic layer based on GIAP-3 (fraction of 0.25–0.50 mm); (b) (*1*) NIAP-18 (fraction of 0.25–0.50 mm), (*2*) NIAP-18 (1/2 grain; hollow cylinder), (*3*) reinforced catalyst based on NIAP-18 (plate), and (*4*) catalytic layer based on NIAP-18 (fraction of 0.25–0.50 mm).

film containing nickel and chromium oxides was formed on the surface of catalysts. This oxide film was incompletely reduced under conditions of reduction in H_2 because of the interaction of nickel oxide with difficult-to-reduce chromium oxide. The XRD and XPS data allowed us to conclude that the interaction of nickel and chromium oxides with the formation of a solid solution (for the composite catalyst based on NIAP-18) occurred at the stage of preparation upon high-temperature calcination (Table 1, Fig. 4b). The effect of chromium oxide on the reducibility of nickel oxide can be related to different oxygen affinities of nickel and chromium. The incorporation of difficult-to-reduce chromium ions into the structure of nickel oxide decreased the reactivity of oxygen and inhibited the reduction of nickel oxide. The increase of the reduction temperature of NiO upon the addition of Cr_2O_3 was demonstrated previously [20, 21]. According to Chizhikov et al. [26], the temperature of the onset of reduction of the $NiCr_2O_4$ compound, which was prepared by the calcination of a mixture of nickel and chromium oxides, was 960°C. A similar increase in the reduction temperature was observed in the case of nickel catalysts supported onto magnesium oxide: the fraction of reduced nickel was 6% after the reduction of a sample, which was calcined at 800°C, at 725°C [27].

It is likely that the reduction of nickel oxide under the action of a reaction atmosphere was responsible for the increase of conversion in the course of the reaction on composite catalysts. In this case, NiO was reduced with the participation of H atoms formed in the reaction rather than with molecular hydrogen. It is evident that, on commercial catalysts, a film of nickel oxide was readily reduced at the stage of reduction and the initial degree of conversion reached a maximum.

A comparison of activities on a unit volume basis showed that, after 30-h testing, the activity of reinforced catalysts was lower than the activity of commercial catalysts by a factor of ~2 (Table 4).[1] A comparison between the activities of commercial and composite catalysts on a unit weight (fraction) basis suggested that the activity of composite catalysts was higher than the activity value that corresponded to the commercial catalyst contents of the composite catalysts. This can be due to the contribution of a nickel metal matrix to the catalytic activity. In the surface layers of this matrix, nickel crystallites are formed from a solid solution of chromium oxide in nickel oxide under the action of a reaction atmosphere. In this case, chromium oxide exerts a stabilizing effect to prevent the agglomeration of nickel crystallites and to increase the extent of dispersion of nickel [19].

Catalytic Activity of Nickel–Platinum Catalysts

The degrees of conversion in the reaction of hydrogen oxidation on the composite nickel–platinum catalyst were comparable with the conversions on the supported platinum catalyst (Table 5). The decrease in the degree of conversion on the reinforced catalyst containing nickel–platinum (with reference to the supported catalyst) was smaller than that in the case of direct proportion to the supported catalyst content of this reinforced catalyst. This may be a consequence of the contribution of nickel and aluminum intermetallides to the catalytic reaction [29].

It is likely that a dramatic increase in the degree of conversion as the temperature was increased to 75°C (Table 5) was due to reaction transition to the diffusion region and the heating of the catalyst surface (surface ignition conditions [30]).

[1] The reaction rate constant at 750°C was evaluated using a first-order equation with respect to methane [28].

Table 4. Catalytic activity of nickel catalysts in the reaction of methane steam reforming

Catalyst	Geometric shape	Methane conversion,* %		Rate constant	
		I*	**II***	cm^3 (g Cat)$^{-1}$ × s^{-1} atm^{-1}**	cm^3 (ml Cat)$^{-1}$ × s^{-1} atm^{-1}***
GIAP-3	Fraction (m = 0.80 g)	75	65	7.5	–
	1/2 grain (m = 2.01 g, V = 0.7 cm^3)	51	49	–	4.5
(7.5% GIAP-3 + 50.3% Ni + 1.2% Cr_2O_3) stainless steel gauze	Plate (m = 2.00 g, V = 0.7 cm^3)	20	50	–	4.7
12.5% GIAP-3 + 85.5% Ni + 2.0% Cr_2O_3****	Fraction (m = 0.80 g)	22	30	1.8	–
NIAP-18	Fraction (m = 0.80 g)	74	69	9.4	–
	1/2 grain (m = 1.46 g, V = 0.7 cm^3)	69	66	–	9.5
(7.5% NIAP-18 + 50.4% Ni + 2.1% Cr_2O_3) stainless steel gauze	Plate (m = 2.23 g, V = 0.7 cm^3)	16	49	–	4.5
12.5% NIAP-18 + 84.0% Ni + 3.5% O_3****	Fraction (m = 0.80 g)	10	36	2.2	–

*I and II refer to the initial value and the value obtained after 30 h for fractions or after 50 h for plates and grains, respectively.

**After 30 h.

***After 50 h.

****Catalytic layer separated from reinforcing gauze.

Kirillov et al. [1] published the results of testing a plate heat-exchange reactor with the use of reinforced catalysts. From these results, it follows that temperature gradients between exothermic and endothermic reaction zones were practically absent.

Thus, this study demonstrated that the nickel-containing reinforced catalysts prepared in accordance with the proposed procedure were active in the reaction of methane steam reforming, whereas the catalysts containing nickel–platinum were active in the reaction of hydrogen oxidation and exhibited high thermal conductivity.

Table 5. Catalytic activity of platinum and nickel–platinum catalysts in the reaction of hydrogen oxidation

Catalyst	Sample weight, g	T, °C	H_2 conversion, %
0.6% Pt/Al_2O_3 (fraction)	0.51	75.0	62
		74.0	50
		63.0	36.5
12% (0.6% Pt/Al_2O_3) + 70.0% Ni + 18.0% Al (fraction)	0.51	75.5	64
		74.5	54
		63.0	36
(7.2% (0.6% Pt/Al_2O_3) + 10.8% Al + 42.0% Ni)/steel gauze (balance)	1.73	75.0	54
		74.5	48

ACKNOWLEDGMENTS

We are grateful to I.I. Bobrova, N.N. Bobrov, V.I. Zaikovskii, N.F. Saputina, and L.G. Simonova for their assistance in performing this study and discussions of the results.

This work was supported by the International Science and Technology Center (project no. 2291).

REFERENCES

1. Kirillov, V.A., Kuzin, N.A., Kulikov, A.V., Fadeev, S.I., Shigarov, A.B., Sobyanin, V.A., *Teor. Osn. Khim. Technol.*, 2003, vol. 37, no. 3, p. 300 [*Theor. Found. Chem. Eng.* (Engl. Transl.), vol. 37, p. 276].
2. Polman, E.A., Der Kinderen, J.M., Thuis, F.M.A., *Catal. Today*, 1999, vol. 467, p. 347.
3. Ismagilov, Z.R., Podyacheva, O.Yu., Pushkarev, V.V., et al., *Stud. Surf. Sci. Catal.*, 2000, vol. 130, p. 2759.
4. Ismagilov, Z.R., Pushkarev, V.V., Podyacheva, O.Yu., et al., *Chem. Eng. J.*, 2001, vol. 82, p. 355.
5. RF Patent 26202, 1996.
6. Danilova, M.M., Kuzin, N.A., Kirillov, V.A., et al., *React. Kinet. Catal. Lett.*, 1999, vol. 69, no. 2, p. 317.
7. *Spravochnik azotchika* (Nitrogen Engineer's Handbook), Mel'nikov, E.Ya., Ed., Moscow: Khimiya, 1986, p. 71.
8. Yagodkin, V.I., Fedyukin, Yu.T., Men'shov, V.N., Ezhova, N.N., and Daut, V.A., *Khim. Prom–st.*, 2001, no. 2, p. 7.
9. Kikuyama, S., Matsukuma, I., Kikuchi, R., et al., *Appl. Catal., A*, 2001, vol. 219, p. 107.

10. *Practical Surface Analysis by Auger and X-ray Photoelectron Spectroscopy*, Briggs, D. and Seah, M.P., Eds., Chichester: Wiley, 1983.
11. Moulder, J.F., Stickle, W.F., Sobol, P.E., and Bomben, K.D., *Handbook of X-ray Photoelectron Spectroscopy*, Eden Prairie, MN: Perkin-Elmer, 1992.
12. Boreskov, G.K., *Zh. Fiz. Khim.*, 1957, vol. 31, no. 5, p. 937.
13. *Powder Diffraction File*, Swarthmore: Joint Committee on Powder Diffraction Standards, no. 47-1019.
14. Danilova, M.M., Kuzin, N.A., Kirillov, V.A., Panchenko, E.A., Meshcheryakov, V.D., Moroz, E.M., and Rudina, N.A., *Kinet. Katal.*, 2002, vol. 43, no. 6, p. 893 [*Kinet. Catal.* (Engl. Transl.), vol. 43, no. 6, p. 830].
15. Babenko, V.S., Buyanov, R.A., and Afanas'ev, A.D., *Kinet. Katal.*, 1979, vol. 20, no. 1, p. 212.
16. Geguzin, Ya.E., *Fizika spekaniya* (Physics of Sintering), Moscow: Nauka, 1967, p.130.
17. Moulder, J.F., Cadot, S., and Marcus, P., *Surf. Sci.*, 2001, vol. 471, p. 43.
18. Moulder, J.F., Catod, S., and Marcus, P., *Surf. Sci.*, 2000, vol. 458, p. 195.
19. *Spravochnik khimika* (Chemist's Handbook), Leningrad: Khimiya, 1971, vol. 1, p. 786.
20. Simonova, L.G., *Cand. Sci. (Chem.) Dissertation*, Novosibirsk: Inst. of Catalysis, 1975.
21. Borisova, M.S., Dzis'ko, V.A., Noskova, S.P., Petrova, N.Z., and Plyasova, L.M., *Kinet. Katal.*, 1971, vol. 12, no. 4, p. 1034.
22. Wang, J.B., Kuo, L.E., and Huang, T-J., *Appl. Catal., A*, 2003, vol. 249, p. 93.
23. Naiborodenko, Yu.S. and Itin, V.I., *Fiz. Goreniya Vzryva*, 1975, vol. 11, no. 3, p. 343.
24. Savitskii, A.P., Martsunova, L.S., Burtsev, N.N., et al., *Izv. Akad. Nauk SSSR, Met.*, 1985, no. 2, p. 191.
25. Vol, A.E., *Stroenie i svoistva dvoinykh metallicheskikh sistem* (Structure and Properties of Binary Metallic Systems), Moscow: Fizmatgiz, 1959, p. 400.
26. Chizhikov, D.N., Gol'dman, B.S., and Kazenas, E.K., *Dokl. Akad. Nauk SSSR*, 1974, vol. 215, no. 1, p. 107.
27. Arena, F., Horrel, B.A., Cocke, L.H., et al., *J. Catal.*, 1991, vol. 132, no. 1, p. 58.
28. Sobyanin, V.A., Bobrova, I.I., Titova, E.Yu., et al., *React. Kinet. Catal. Lett.*, 1989, vol. 39, no. 2, p. 443.
29. Boreskov, G.K., Slin'ko, M.G., and Filippova, A.G., *Dokl. Akad. Nauk SSSR*, 1953, vol. 92, no. 2, p. 353.
30. Frank-Kamenetskii, D.A., *Diffuziya i teploperedacha v khimicheskoi kinetike* (Diffusion and Heat Transfer in Chemical Kinetics), Moscow: Nauka, 1987.